

Ferroelectric dynamic-field-driven nucleation and growth model for predictive materials-to-circuit co-design

Yi Liang,^{1,5,*} Tony Chiang,¹ Megan K. Lenox,² John J. Plombon,³ Jon F. Ihlefeld,^{2,4} Wenhao Sun,¹ and John T. Heron^{1,5,*}

¹Department of Materials Science and Engineering,

University of Michigan, Ann Arbor, MI 48109, USA

²Department of Materials Science and Engineering,

University of Virginia, Charlottesville, VA 22904, USA

³Technology Research, Intel Corporation, Hillsboro, OR 97124, USA

⁴Charles L. Brown Department of Electrical and Computer Engineering,

University of Virginia, Charlottesville, VA 22904, USA

⁵The Ferroelectronics Laboratory, University of Michigan, Ann Arbor, MI 48109, USA

* Corresponding authors: liangyy@umich.edu, jtheron@umich.edu

Real ferroelectric devices operate under mixed and distorted time-varying voltages, yet the standard nucleation-growth frameworks used to interpret ferroelectric switching — most notably the Kolmogorov-Avrami-Ishibashi (KAI) and nucleation-limited switching models (NLS) — are derived under the critically limiting assumption of a constant electric field. Thus, the prevailing interpretation of ferroelectric switching dynamics fails under real operating conditions. Here we introduce a compact dynamic-field-driven nucleation and growth (DFNG) model that enables quantitative fits to switching transients across multiple ferroelectric materials to extract time-varying domain wall velocity and growth dimensionality, even under arbitrary voltage waveform. This capability then motivates its use in device modeling under complex signals spanning disparate time and frequency scales. Coupling the compact model to application-related waveforms facilitates a predictive materials-circuit co-design framework by linking nucleation and growth parameters to memory window, disturb error, speed, and energy dissipation for next-generation ferroelectric technologies.

Main

The low-power, high-speed, and non-volatile characteristics of ferroelectric materials have enabled device concepts^{1–3} that can surpass conventional CMOS technologies^{4–6}. Key to the ferroelectric computing technologies is the manipulation of polarization under ultrafast mixed-frequency and time-dependent voltage waveforms (Fig. 1a). The time evolution of polarization transient composes the intricate metrics of ferroelectric materials and devices, such as latency, energy, disturb errors, and readout signals. To assist high throughput material design and to optimize device operation protocols, a compact model is needed to predict physical response of ferroelectrics under the dynamic electric fields.

Existing models, however, are unable to describe the nucleation and growth processes which drive ferroelectric switching under a time-varying voltage, largely because ferroelectric polarization evolution is hysteretic and depends on the full history of applied electrical stimuli. For example, the seminal Kolmogorov-Avrami-Ishibashi (KAI) model^{7–9} provides an explicit description of the polarization transient under a constant applied voltage. Even when a voltage dependence is inappropriately forced, the polarization is only dependent on instantaneous voltage value and ignores the prior voltage path (Fig. 1b and Supplementary Note 1). This deficiency is also found in the nucleation-limited switching (NLS) model¹⁰, which simulates a switching event from a distribution of local nucleation times under a constant applied field and neglects domain growth. In addition, the distribution function in the NLS model is ad hoc and thus usually leads to overfitting of experimental transients, thereby overlooking physical rationalization. On the other hand, time-dependent Ginzburg-Landau-Devonshire^{11–13}, Preisach, or other equivalent-circuit models, can be numerically driven by any waveform, but they neglect the necessary nucleation and growth physics or are generally too complex to serve as compact, closed-form fitting tools for experimental transients.

In this work, we present a dynamic-field-driven nucleation and growth (DFNG) model that is universally applicable to distinct materials and arbitrary waveforms (Fig. 1b). We first demonstrate the capability by self-consistently fitting experimental polarization switching transients for polycrystalline $\text{Hf}_{0.5}\text{Zr}_{0.5}\text{O}_2$ (HZO) and single-crystalline BaTiO_3 (BTO) thin films with as few as 3 parameters. The model robustly extracts intrinsic materials parameters (growth dimension, nucleation density, and Merz activation field), even when there are mixed time-scale changes in the voltage profile due to the rise time of electronics (10–100 ps) and slower circuit parasitic effects (1–10 ns), making materials-level inference possible even under practical measurements with non-idealities. We then derive domain wall velocity and domain size of HZO, which motivates a speculation of domain-growth-limited switching mechanism with instantaneous nucleation corroborated by experimental findings, contrary to the proliferated belief of nucleation-limited

switching. Furthermore, the model generates realistic material response to time-varying mixed-frequency waveforms which can readily incorporate with circuit-level modeling to optimize circuit design and operation protocols. Finally, the model is used to map material parameters to hysteresis loops and technology metrics, providing insight on design principles based on application requirements. Together, our study for the first time establishes a universal, physics-grounded framework that links nucleation and growth dynamics to device-level performance metrics, offering a foundation for elucidating material fundamentals and a rational co-design platform for next-generation ferroelectric technologies.

A compact yet generalized nucleation and growth model

Our DFNG model extends the traditional Avrami theory of nucleation and growth to capture the ultrafast voltage profiles driving a ferroelectric phase transformation by including two important physical considerations: 1) Nucleation is either instant or adopt a changing steady-state nucleation rate, whose bulk driving force depends on the time-dependent voltage profile; 2) a non-linear voltage-dependent growth rate based on Merz law¹⁴.

We build our derivation from Cahn's time-cone model¹⁵, which relates the transformed fraction, $f(t)$, of a system undergoing a phase transition to the number of nuclei, $\langle N(t) \rangle$, in a cone of space-time that precedes the time and point of space where nucleation may occur (reverse time cone) by

$$f(t) = 1 - \exp[-\langle N(t) \rangle] \quad (1)$$

Where,

$$\langle N(t) \rangle = \gamma \int_0^t J(\tau) \left[\int_{\tau}^t v(t') dt' \right]^d d\tau \quad (2)$$

Here d is domain growth dimension, and γ is the geometric factor of domain growth, e.g. $\gamma = 1$ for 1-dimension, π for 2-dimension, and $\frac{4}{3}\pi$ for 3-dimension. γ and d can be applied to mixed dimensions. $v(t')$ is the domain wall velocity at time t' , dictated by Merz law $v(t') = v_0 \exp\left[\frac{-V_a}{V(t')}\right]$, where v_0 is the domain wall velocity at infinite voltage approximated as the speed of sound, and $V(t')$ is the instantaneous voltage. $J(\tau)$ is the nucleation rate at time τ . For instantaneous nucleation, $\langle N(t) \rangle$ is acquired with $J(\tau) = \rho_1 \delta(0)$:

$$\langle N(t) \rangle = A^d \left[\int_0^t \exp\left[-\frac{V_a}{V(t')}\right] dt' \right]^d, \quad (3)$$

where $A^d = \gamma \rho_1 v_0^d$, and ρ_1 is the density of pre-existing nuclei. Thus, parameter A is an indicator of instantaneous nucleation density. For the homogeneous nucleation rate governed by a thermodynamic barrier, we adopt an expression of the nucleation probability from the Janovec-Kay-Dunn model^{16,17}, which leads to the following expression for $\langle N(t) \rangle$:

$$\langle N(t) \rangle = B^d \int_0^t \exp \left[-\frac{V_a + \sigma'^2}{V(\tau)} \right] \left[\int_{\tau}^t \exp \left[-\frac{V_a}{V(t')} \right] dt' \right]^d d\tau, \quad (4)$$

where B is associated with homogeneous nucleation density, and σ' is associated with domain wall energy. Detailed derivation can be found in Supplementary Note 2. The integral forms in eqn. (3) and (4) preserve voltage path dependent switching transients.

Material parameters from measurements in dynamic field across materials

We begin by applying the model to the HZO system. We experimentally measure ferroelectric switching transients in 3- μm diameter capacitors by simultaneously acquiring the voltage across the ferroelectric capacitor (V_{FE}), the ferroelectric switching current df/dt (normalized by $2P_S$), and the polarization (transformed fraction f when normalized by $2P_S$) as a function of time (Fig. 1a, c). Details of the transient measurements are given in the Methods section and elsewhere¹⁸. We find that the model best fits the experimental data when an instantaneous nucleation rate is used (Fig. S1), indicating the presence of preexisting nuclei. These nuclei are possibly permanent dipoles formed by bound charges at the electrode-insulator interface, grain boundaries and phase boundaries (hence heterogeneous). The fit yields $d = 0.699 \pm 0.003$, $V_a = 12.75 \pm 0.09$ V, $A = 3236 \pm 191$ ns⁻¹. These parameters are extracted via a global fit across four different supply voltage profiles while feeding the measured real-time voltage as an input. This ensures the extracted parameters are intrinsic to the material, independent of the variance in applied voltage. The values of these parameters reflect their physical origins and will be discussed in a few paragraphs.

The expression of eqn. (3) for HZO is compact, as it only involves three parameters A , V_a , and d , yet able to capture the full experimental switching transient particularly through the rapid voltage variations that occur at sub-ns and ns scales (Fig. 1c). In real circuits, the rise of the voltage pulse is skewed by the finite rise time of the pulse generator and the dielectric current, which here is ~ 200 ps. Interestingly, ferroelectric switching occurs during this rapid voltage rise and produces a dynamic Avrami exponent (exceeding 4) at the beginning. The DFNG model captures this behavior and outputs a large initial Avrami exponent because the domain wall velocity accelerates non-linearly upon the rapid rise of the voltage. After, the Avrami exponent relaxes back to an interpretable growth dimension value as the voltage settles. This

result indicates that apparent super-physical Avrami exponents frequently reported in the literature naturally arise from dynamic-field effects. After the initial voltage rise, significant ferroelectric switching current is generated and flows through the series resistor in the circuit for larger voltage amplitudes, leading to a sluggish rise to the set voltage (between the green and grey dashed lines in Fig. 1c). This distortion of the voltage waveform spans through almost the entire switching process, which highlights the necessity of incorporating a time-dependent voltage for modeling ferroelectric switching transients. The deviation from the ideal square pulse also implies the common misuse of the conventional KAI and NLS model where constant voltage is assumed. Contrarily, our model allows for robust physical parameter extraction even when there are ultrafast changes in the voltage profile due to the rise time of the electronics (10-100 ps scale) and slower circuit parasitic effects (1-10 ns scale) making possible materials-level inference under unideal measurement conditions.

To demonstrate universality, we apply the model to single-crystalline BTO with both heterogeneous and homogeneous nucleation included, by summing eqn. (3) and (4), and involving 5 fit parameters. The model fits to the whole transient of a 3- μ m BTO capacitor despite rapid voltage variations and for all voltage profiles (Fig. S2). A low V_a of ~ 0.5 V, sparse nucleation density of $\sim 10^4$ nm^{-d}, and domain wall energy of 4.4 mJ/m² are determined and consistent with the single-crystalline nature of BTO (Supplementary Note 3).

Uncovering microscopic switching mechanisms from model analysis

Nucleation sites, domain wall velocity, and domain sizes that can be visualized or inferred with modern techniques such as piezoresponse force microscopy and advanced transmission electron microscopy¹⁹⁻²², serve as observable quantities to verify physics postulated in theoretical models. With the DFNG model, we derive physical values for these quantities and further posit a growth-limited switching mechanism in HZO, contrary to the popular NLS picture, which is further corroborated by a recent *operando* electron holography experiment²⁰.

By assuming a v_0 value of 6000 m/s²³, domain wall velocity v , nucleation rate J , and domain radius r can be directly output from the model (Fig. 2). The domain wall velocity of HZO (Fig. 2b) during switching increases from 0 to 1.2 m/s (low voltage, light purple) and 14.4 m/s (high voltage, dark purple) resulting from the high activation field for depinning in a defective medium. Despite the slow growth rate, HZO exhibits a comparable switching time to BTO because of a much higher nucleation density (Fig. 2c). Heterogeneous nucleation density of HZO is estimated to be ~ 1 nm^{-d}. Note that the heterogeneous nucleation density is the volumetric number of nucleation sites averaged over the device area. Therefore, multiple nucleation defects can exist in one grain as they reside at the grain boundaries, intragranular phase

boundaries, and the ferroelectric-electrode interface. The domain wall velocity also leads to distinct profiles in time cones and domain sizes (Fig. 2d). In contrast to the straight time cone profile in the conventional KAI model, real materials possess a curved lateral surface due to a time-varying domain wall velocity. Domain radius r of HZO is estimated to be several nanometers. The small domain size of HZO provides an effective alternative to the NLS model's claim that domain wall motion is confined within a grain. Our model reveals that nucleation is instantaneous and domain walls are mobile across grain boundaries albeit encountering a high Merz barrier. Therefore, a switching paradigm that is limited by domain growth (Fig. 2d, top right) must replace the NLS picture (Fig. 2d, bottom right) where domain wall mobility is bounded by polycrystallinity and granularity. Notably, the domain size of a few nanometers and the lateral growth of domains to the neighboring grain are confirmed by electron holography²⁰, validating the physical foundation of our model.

Polarization behavior under realistic complex circuit voltages

Nowadays, ferroelectric materials have attracted significant interest for neuromorphic computing as a compute-in-memory (CiM) technique to overcome the von Neumann bottleneck, as the stored polarization charge naturally encodes synaptic weights. FeFET (ferroelectric field effect transistor), FeCap (ferroelectric capacitor), and FTJ (ferroelectric tunnel junction) crossbar arrays are developed for non-destructive readout of the states^{24–26}. The operation of these devices requires deliberately designed mixed signal waveforms to achieve correct and efficient functionality²⁷. The previous void of a compact and physical model of polarization switching under dynamic electric field hinders the incorporation of ferroelectric components into circuit-level modeling and thus optimization. Here we show that the DFNG model can produce realistic material responses to a potential complex dynamic waveform.

We use the mixed signal nature of a small signal capacitance-voltage $C(V)$ hysteresis loop measurements as an example (Fig. 3), where a low-amplitude AC signal superimposed on a DC bias is used. This measurement well represents the complexity of the waveform used in real-world circuits and the small-signal capacitance is recently proposed as an efficient readout mechanism for charge-based neuromorphic computing^{28,29}. In Fig. 3a, the model produces the ideal hysteresis, where leakage and internal fields are ignored. It replicates the empirical trend that increased AC frequency leads to a higher coercive field and lower peak capacitance defined by the $C(V)$ loops. Moreover, the polarization (f) and current (df/dt) traces in Fig. 3b essentially indicate the accumulated charges and current flow which are potential readout signals in a circuit with a ferroelectric element. We note that the polarization and current drift during the AC oscillation causes a time-dependent variation in the readout capacitance values and may compromise the

read margin if multi-level operation is performed on the FeCap. The variance of capacitance is most significant around the DC voltage where polarization switching occurs most rapidly.

Materials-to-circuit co-design platform enabled by the model

We next present a potential routine for evaluating material eligibility for technologies and accelerating synthesis optimization. From a ferroelectric material synthesis prospective, polarization-voltage $P(V)$ hysteresis measurement is the most typical diagnosis. We therefore vary the material parameters and map the corresponding $P(V)$ loops in Fig. 4a (Supplementary Note 4 and Fig. S3, Fig. S4). It qualitatively shows that decreasing heterogeneous nucleation sites or increasing depinning barrier leads to wider loops, and that decreasing growth dimension leads to skewed loops. Meanwhile, pulse operation (Fig. S5) and high frequency ramps, as frequently used waveforms in applications, are performed to extract metrics of interest. We then grade the material parameters following the procedure below (and Supplementary Note 4):

- 1) Determinism under CMOS conditions: 99% switching fraction should be completed within 10 ns (delay) with a pulse amplitude (V_{min}) ≤ 1.5 V⁴.
- 2) Memory stability against disturb: characterized by the polarization loss fraction Δf under a write disturb pulse in the $V_{DD}/2$ scheme³⁰. Nominally $\Delta f \leq 5\%$ is acceptable for memory device such as FeRAM (ferroelectric random-access memory), and $\Delta f \leq 1\%$ for CiM devices as they encounter more frequent write operations.
- 3) Energy and delay for CiM under write operation.
- 4) Memory window for FeCaps³¹: $C_{norm} = \left(\frac{df}{dV}\right)_{f=0.5} = \frac{1}{P_S t_{FE}} \epsilon_{FE}$. ϵ_{FE} is the dielectric constant of the ferroelectric (subtracting the linear part).
- 5) Read margin / Memory window for FeFETs³²: $V_C = V_{f=0.5}$.

We locate the loop of the current HZO sample according to its fit parameters (Fig. 4a, purple star). This immediately suggests that a modest increase in nucleation density and growth dimension would adapt the material for a CiM application (orange star). Physically, such tuning could be achieved by introducing small dipole clusters and removing some grain boundaries, as charged defects act as heterogeneous nucleation sites while mesoscopic grain boundaries truncate the time cone and reduce growth dimension. The corresponding ranges of energy and delay are indicated by the red dots beside the loop. The orange star matches the loop in Fig. 4a to a FeFET application with corresponding metrics in Fig. 4b. Furthermore, Fig. 4b provides the tunable range and pairwise correlation of the metrics which allow inverse design strategy and fast estimation of performance. For example, FeFETs favor materials with large V_C , outlined by the

orange box. These selected sets are bound to good control of memory stability and tight distribution of energy dissipation, leaving delay the only variable of concern. Similarly, FeCap devices favor high capacitances outlined by the green box. However, achieving these capacitance values requires high growth dimension ($d > 1.6$) and low Merz barrier ($V_a < 4$ V), which can be extremely demanding in polycrystalline materials. More discussion is attached in Supplementary Note 5. Other general trends can also be concluded. The correlation between V_{min} , delay, and energy indicates that material parameters enabling lower operating voltages tend to reduce the switching energy, as the switching time decreases exponentially. The relation between Δf and other metrics is less defined as it is subject to a different pulse amplitude, suggesting that disturb immunity cannot be inferred from other measurements and requires a dedicated examination.

Conclusion

While the thriving of complex atomic-scale computational methods has greatly enriched fundamental understanding of ferroelectric switching mechanisms^{33–36}, the DFNG model presented in this work is compact yet able to serve as a complementary framework that links physical parameters related to microscale structure to experimental observables such as such as realistic switching transients, domain wall motion, and domain size. It enables extraction of material parameters under arbitrary time-dependent waveform and fast evaluation of technology metrics. We envision the model to be a powerful tool for performance-guided materials design and circuit-level optimization, thereby accelerating the development of next-generation ferroelectric computing technologies.

Methods

Thin Film Growth

The $\text{Hf}_{0.5}\text{Zr}_{0.5}\text{O}_2$ (W 20 nm/HZO 10 nm/W 50 nm) film was grown using plasma-enhanced atomic layer deposition on an undoped (001)-oriented silicon substrate, with the bottom and top tungsten layers deposited by DC magnetron sputtering³⁷. The film was crystallized at 600 °C for 30 seconds via rapid thermal annealing in a dynamic N_2 atmosphere at atmospheric pressure. The epitaxial BaTiO_3 (SrRuO_3 20 nm/BTO 20 nm/ SrRuO_3 50 nm) was grown by pulsed laser deposition on a (110)-oriented DyScO_3 single crystal substrate.

Ferroelectric Capacitors Fabrication

The ferroelectric capacitors were fabricated using a combination of E-beam lithography and optical photolithography. A negative ma-N 2405 E-beam resist was spun on the trilayer film stack and exposed using a JEOL JBX-6300FS electron beam lithography system to serve as an etch mask to define the capacitor size. Then the sample was etched down to the bottom electrode with ion mill (Nanoquest II) to create self-aligned top electrode / ferroelectric islands. The sample was backfilled with 140 nm SiO_2 using magnetron sputtering (PVD 75 Proline, Lesker) for low κ isolation between the top and bottom electrodes. Next, a series of photolithography steps were performed to pattern bottom electrodes and lift-off ground planes. Finally, gold (300 nm)/titanium (10 nm) top contact pads were deposited with an E-beam evaporator.

Ultra-fast Ferroelectric Switching Measurements

Ultra-fast measurements were performed in an RF probe station. Ground-Signal-Ground probes (Model 40A, GGB) and low loss RF cables (SF526S/11PC35, HUBER+SUHNER) were used to transmit waveforms to and receive current response from the device. The voltage pulse train was generated by a pulse generator with a rise time down to 100 ps, connected to the top electrode, while the signal was recorded with a 13 GHz oscilloscope with a 50 Ω input, connected to the bottom electrode. With this setup, the current in the series RC circuit can be determined using the oscilloscope 50 Ω internal loading. For real-time voltage monitoring, the high-impedance probes were landed at the top and bottom electrodes to capture the differential voltage across the capacitor. All measurements were conducted in real-time with averaging over three single-shot measurements. To probe the ferroelectric switching transients, a reset pulse with negative polarity was first applied, followed by a positive-up (PU) pulse train. Each pulse width was 1 μs . The ferroelectric current was then extracted by subtracting the current during the U pulse (dielectric current and resistive current) from the current during the P pulse (ferroelectric current, dielectric current and resistive current).

Numerical Model and Fitting

Equation (1-4) and equation (S5) in Supplementary were used to generate f , df/dt as a function of time t and $\ln(-\ln(1 - f))$ as a function of $\ln t$. Time and real-time voltage involved in the equations were experimental values. The slope of the dataset $(\ln(-\ln(1 - f)), \ln t)$ is the classical Avrami exponent. The square errors between model generated values and experimental values under four measured voltage waveforms were summed and a differential evolution algorithm was performed to find the parameter set that gave the global minimum of the square error sum. We noticed that the data points during the initial ~ 200 -ps voltage rise were usually underweighted as they only occupied a smaller portion of time compared to the entire switching duration. To correct for this and to have the model properly reflect the switching kinetics at any stage, we added four times more weight to these data points than the others. The fit error was calculated by sampling locally around the global minimum using least square error algorithm.

Data availability

All data that supports the findings of this study are available from the corresponding author on reasonable request.

A meme summarizing part of this work can be found on <https://ferroelectronicslab.com/memes/>

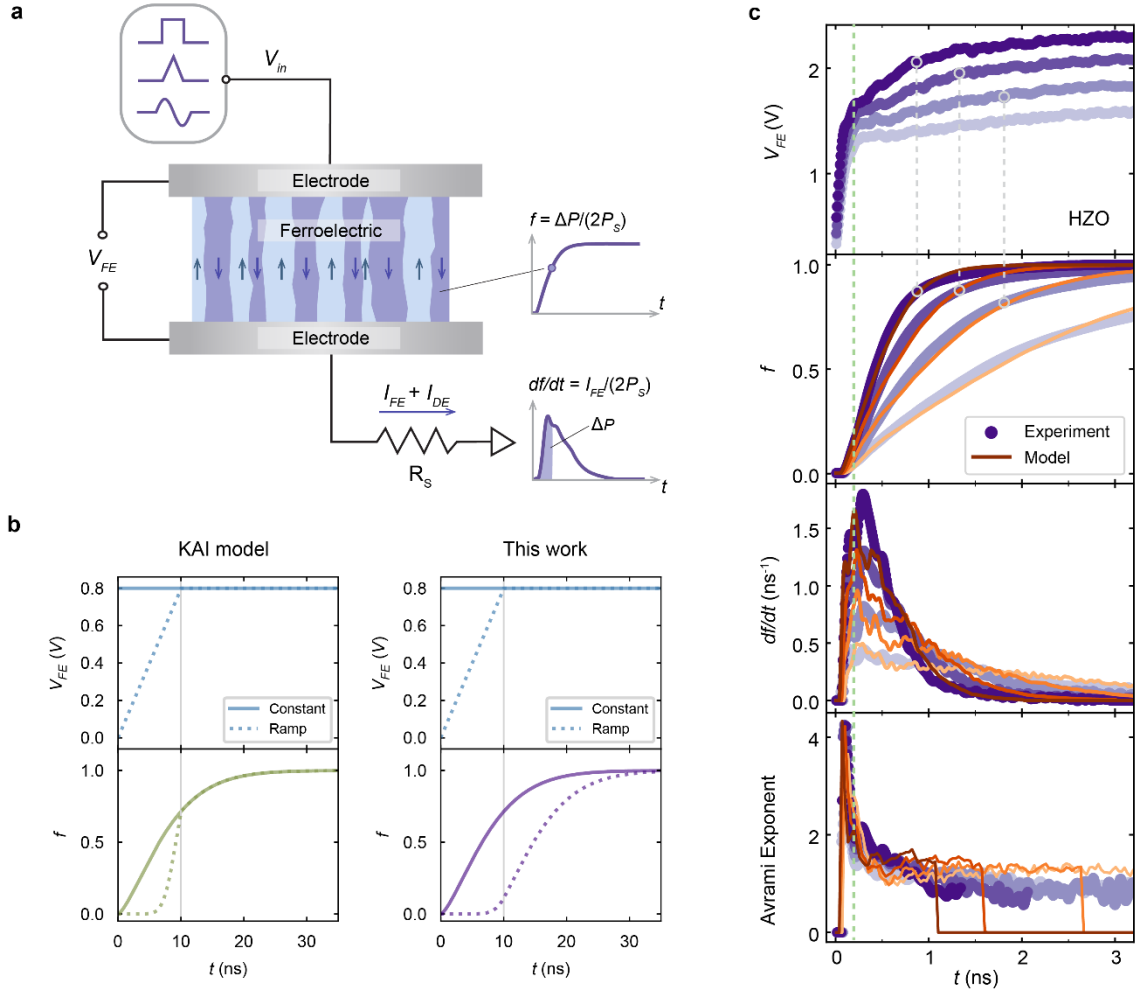


Fig. 1: Ferroelectric switching transients under dynamic electric fields. **a**, A schematic of a ferroelectric capacitor driven by various time-dependent voltage waveforms (V_{in}). Assuming the ferroelectric material is preset to an up-polarized state (blue) before $t = 0$, the waveform induces partial switching via the nucleation and growth of down-polarized domains (purple). The voltage across the ferroelectric capacitor (V_{FE}) and the current transient, including ferroelectric switching current (I_{FE}) and linear dielectric current (I_{DE}) are measured. By integrating I_{FE} and normalizing it to spontaneous polarization (P_s), the instantaneous switched (transformed) fraction (f) can be determined. **b**, Illustration of the error from a naive voltage-dependent KAI model contrasted with the DFNG model presented here. Given a constant applied voltage (solid lines) and voltage ramp to the same set point (dashed lines). The KAI model produces a polarization transient insensitive to the ramp history, in contrast to the DFNG model. **c**, Experimental V_{FE} , f , normalized I_{FE} (df/dt), and Avrami exponent over time (purple) of a 3- μm -diameter polycrystalline HZO capacitor along with a 3-parameter DFNG model fit (orange). The green dashed line marks the end of the fast voltage ramp of the supply (~ 200 ps). The region between the green and grey dashed lines indicates waveform distortion due to a circuit effect. The grey circles mark the corresponding transformed fraction when the voltage saturates to the setpoint. Notably, most switching occurs under a time-varying voltage beyond the validity of traditional nucleation and growth models. The DFNG model accurately reproduces these transients and captures the evolving Avrami exponent, enabling physical interpretation beyond fixed growth dimensionality.

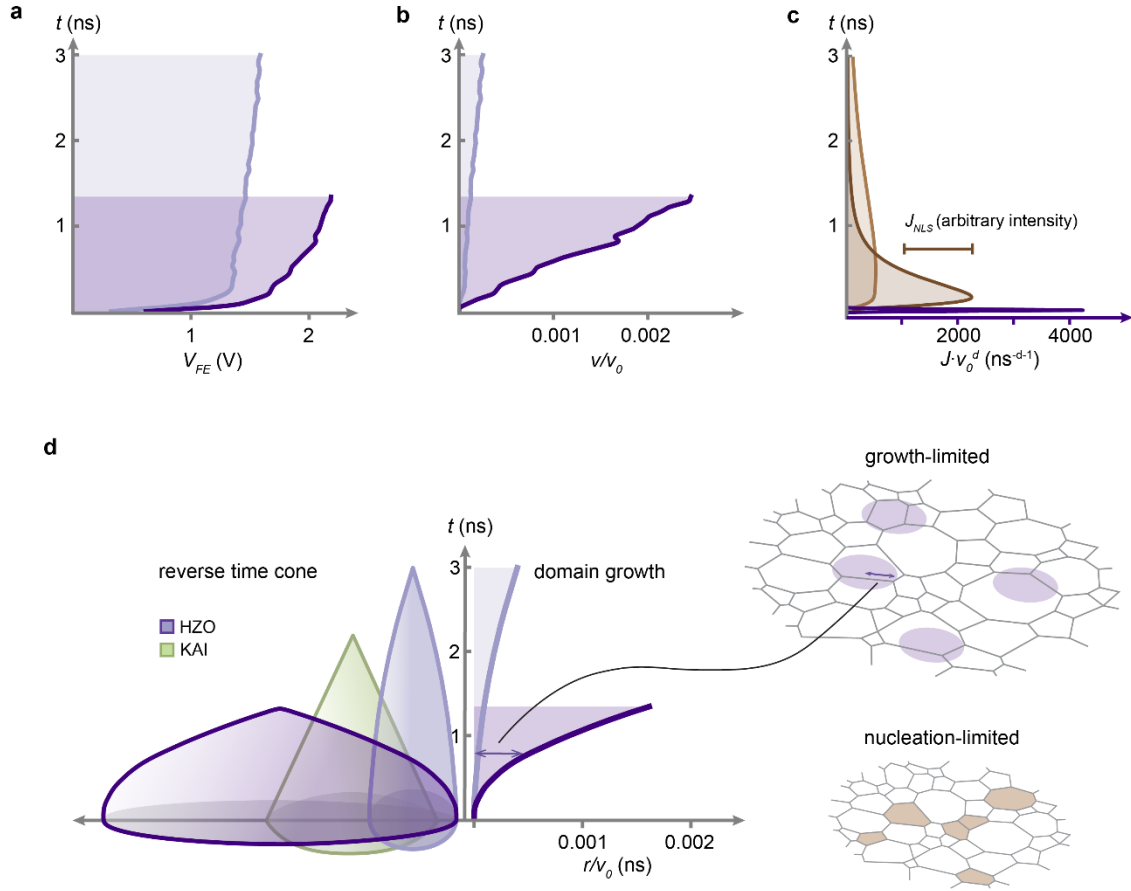


Fig. 2: Time-dependent voltage driven domain nucleation and growth. **a**, Representative experimental time-dependent voltage waveforms across the HZO ferroelectric capacitor. The darker curves deviate more from a square pulse than the lighter curves due to the more pronounced circuit effect. **b**, Extracted domain wall velocity (normalized). The domain wall velocity of HZO roughly increases linearly in time. **c**, Extracted nucleation rate (normalized) of HZO in comparison with a qualitative nucleation profile derived from the NLS (nucleation-limited switching) model. **d**, Extracted reverse time cones and transformed domain radii. In real materials, the time-varying domain wall velocity leads to a curved lateral surface of the reverse time cone. In the idealized KAI model (green), the cone has a straight profile due to its limiting assumptions. Our model reveals that the transformed domain can grow to a radius of a few nanometers, which is comparable to the grain size, but is not restricted inside a grain (top right schematic). In contrast, the NLS model assumes that the domain wall is stagnated by the grain boundary (bottom right schematic). The colored areas are the transformed regions.

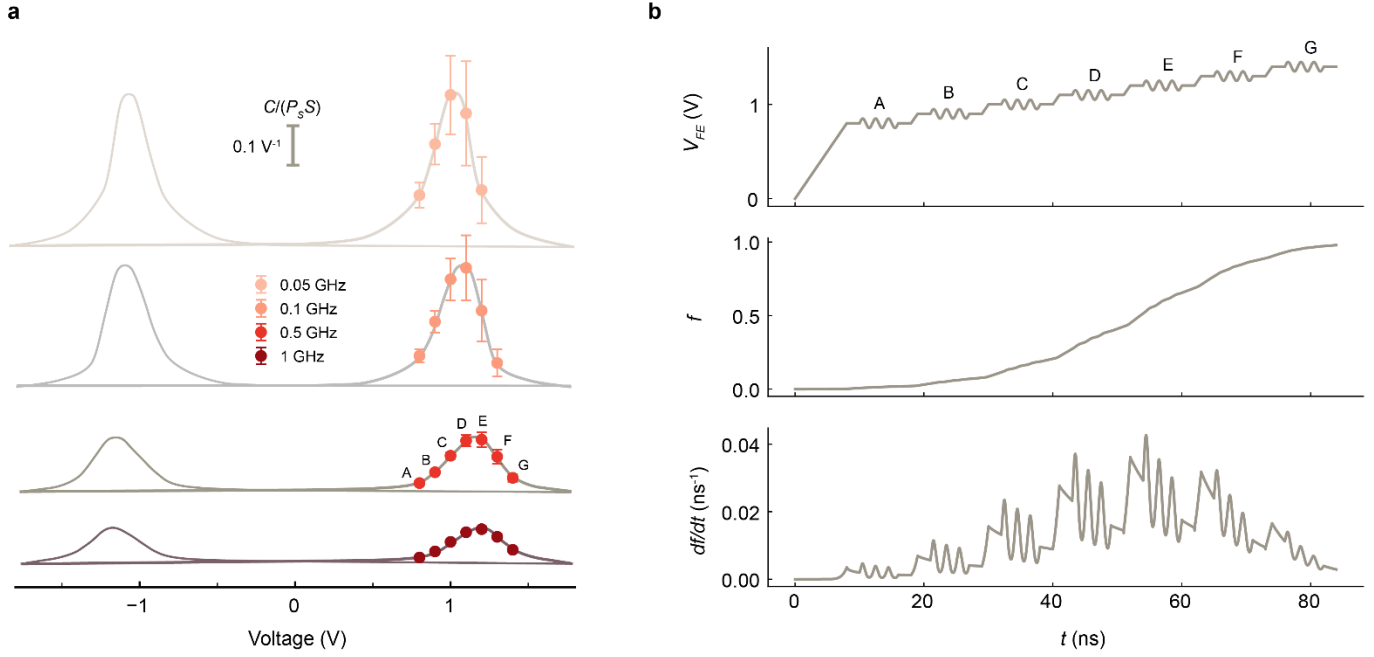


Fig. 3: Mixed-signal simulation: small-signal capacitance. **a**, Simulated frequency-dependent capacitance-voltage $C(V)$ hysteresis. Red dots with error bars are output from the model. Grey curves are guide to eyes. **b**, Assumed waveform (V_{FE}) used to acquire peak capacitance, transformed fraction (f), and normalized current (df/dt), corresponding to $C(V)$ data points at 0.5 GHz in (a). The first three oscillations in the voltage and current are used to generate mean capacitance values and standard deviations. The model captures $C(V)$ hysteresis as well as empirically known behavior such as the decrease in the DC voltage at peak capacitance with decreasing frequency and decreasing peak capacitance with increasing AC frequency. The model also illustrates that polarization drift may lead to significant variance in $C(V)$ data. The model can handle arbitrary mixed voltages spanning orders of magnitude in time and frequency scales.

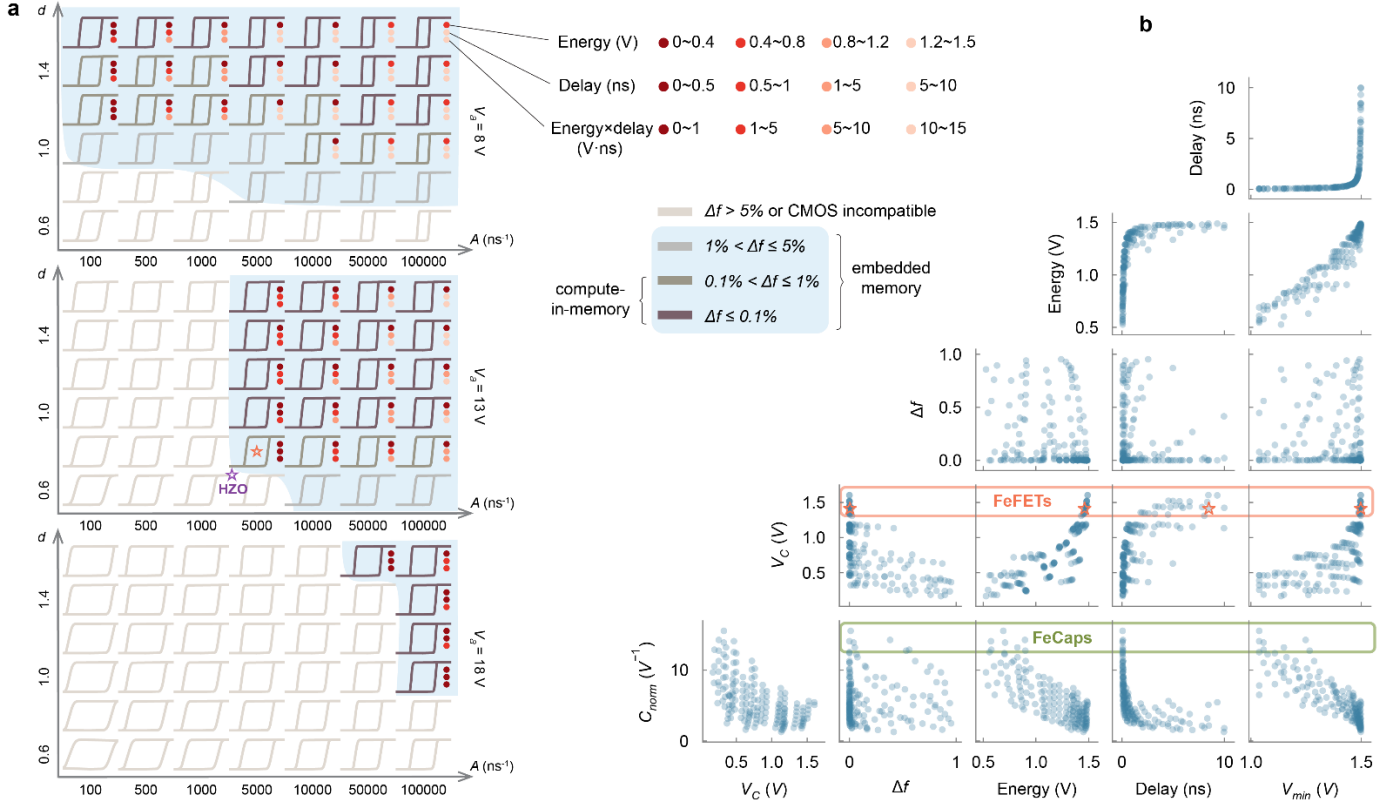


Fig. 4: Mapping material design space to application metrics. **a**, Hysteresis loops generated in a segment of model parameter space using a 1 MHz triangular waveform. The same material parameter sets are used to extract application metrics. We grade each loop according to nominal CiM and embedded memory application standards, illustrated in the legend. The values for energy and capacitance are normalized by polarization and capacitor area. **b**, The correlation between application metrics for CiM devices. The orange box selects parameter sets that render a relatively large V_c and hence sufficient read margin for FeFETs. The green box selects parameter sets that allow a relatively large C_{norm} , which is the memory window in FeCap devices. Orange stars in (b) label a representative parameter set suitable for FeFET and correspondingly in (a) indicates a possible modification direction of the current HZO sample (purple star) for such application. However, modifying it for FeCaps require demanding conditions and hence may not be ideal. Notations used: Δf : normalized polarization loss due to $V_{DD}/2$ write disturb; C_{norm} : normalized peak differential capacitance, $\sim \frac{df}{dV}$; V_c : coercive voltage; V_{min} : minimum pulse amplitude to reach 99% switched fraction within 10 ns.

Reference

1. Martin, L. W. & Rappe, A. M. Thin-film ferroelectric materials and their applications. *Nat. Rev. Mater.* **2**, 16087 (2016).
2. Wang, D., Hao, S., Dkhil, B., Tian, B. & Duan, C. Ferroelectric materials for neuroinspired computing applications. *Fundam. Res.* **4**, 1272–1291 (2024).
3. Wang, J. *et al.* Ferroelectric domain-wall logic units. *Nat. Commun.* **13**, 3255 (2022).
4. Khan, A. I., Keshavarzi, A. & Datta, S. The future of ferroelectric field-effect transistor technology. *Nat. Electron.* **3**, 588–597 (2020).
5. Mikolajick, T., Schroeder, U. & Slesazeck, S. The Past, the Present, and the Future of Ferroelectric Memories. *IEEE Trans. Electron Devices* **67**, 1434–1443 (2020).
6. IEEE International Roadmap for Devices and Systems. *Beyond CMOS and Emerging Materials Integration*. (2023) doi:10.60627/0P45-ZJ55.
7. Kolmogorov, A. N. On the Statistical Theory of Crystallization of Metals [in Russian]. *Izv Akad Nauk SSSR Ser Mat* **3**, 355–359 (1937).
8. Avrami, M. Kinetics of Phase Change. I General Theory. *J. Chem. Phys.* **7**, 1103–1112 (1939).
9. Ishibashi, Y. & Takagi, Y. Note on Ferroelectric Domain Switching. *J. Phys. Soc. Jpn.* **31**, 506–510 (1971).
10. Tagantsev, A. K. Non-Kolmogorov-Avrami switching kinetics in ferroelectric thin films. *Phys. Rev. B* **66**, (2002).
11. L. D. Landau & I. M. Khalatnikov. On the anomalous absorption of sound near a second-order phase transition point. *Dokl. Akad. Nauk SSSR* 469–472 (1954).
12. Devonshire, A. F. XCVI. Theory of barium titanate: Part I. *Lond. Edinb. Dublin Philos. Mag. J. Sci.* **40**, 1040–1063 (1949).
13. Devonshire, A. F. CIX. Theory of barium titanate—Part II. *Lond. Edinb. Dublin Philos. Mag. J. Sci.* **42**, 1065–1079 (1951).
14. Merz, W. J. Domain Formation and Domain Wall Motions in Ferroelectric BaTiO₃ Single Crystals. *Phys. Rev.* **95**, 690–698 (1954).
15. Cahn, J. W. The Time Cone method for Nucleation and Growth Kinetics on a Finite Domain. *MRS Online Proc. Libr.* **398**, 425–437 (1995).
16. Janovec, V. On the theory of the coercive field of single-domain crystals of BaTiO₃. *Cechoslov- Fiz. Zurnal* **8**, 3–15 (1958).

17. Kay, H. F. & Dunn, J. W. Thickness dependence of the nucleation field of triglycine sulphate. *Philos. Mag. J. Theor. Exp. Appl. Phys.* **7**, 2027–2034 (1962).
18. Chiang, T. *et al.* Material-Limited Switching in Nanoscale Ferroelectrics. Preprint at <https://doi.org/10.48550/arXiv.2507.12353> (2025).
19. Gao, P. *et al.* Revealing the role of defects in ferroelectric switching with atomic resolution. *Nat. Commun.* **2**, 591 (2011).
20. Zhang, L. *et al.* Mapping electric fields and observation of ferroelectric domain switching in hafnia-zirconia devices by electron holography. *Nat. Commun.* **16**, 11233 (2025).
21. Ahn, Y. & Son, J. Y. Scaling Effects on Ferroelectric Polarization Switching and Activation Electric Field in Epitaxial Hf_{0.5}Zr_{0.5}O₂ Nanodots. *Adv. Funct. Mater.* **n/a**, e11839.
22. Nelson, C. T. *et al.* Domain Dynamics During Ferroelectric Switching. *Science* **334**, 968–971 (2011).
23. Fields, S. S. *et al.* Compositional and phase dependence of elastic modulus of crystalline and amorphous Hf_{1-x}Zr_xO₂ thin films. *Appl. Phys. Lett.* **118**, 102901 (2021).
24. Beyer, S. *et al.* FeFET: A versatile CMOS compatible device with game-changing potential. in *2020 IEEE International Memory Workshop (IMW)* 1–4 (2020). doi:10.1109/IMW48823.2020.9108150.
25. Mukherjee, S. *et al.* Pulse-Based Capacitive Memory Window with High Non-Destructive Read Endurance in Fully BEOL Compatible Ferroelectric Capacitors. in *2023 International Electron Devices Meeting (IEDM)* 1–4 (2023). doi:10.1109/IEDM45741.2023.10413879.
26. Luo, Z. *et al.* High-precision and linear weight updates by subnanosecond pulses in ferroelectric tunnel junction for neuro-inspired computing. *Nat. Commun.* **13**, 699 (2022).
27. Oh, S., Hwang, H. & Yoo, I. K. Ferroelectric materials for neuromorphic computing. *APL Mater.* **7**, 091109 (2019).
28. Yu, E., K, G. K., Saxena, U. & Roy, K. Ferroelectric capacitors and field-effect transistors as in-memory computing elements for machine learning workloads. *Sci. Rep.* **14**, 9426 (2024).
29. Luo, Y.-C. *et al.* Experimental Demonstration of Non-volatile Capacitive Crossbar Array for In-memory Computing. in *2021 IEEE International Electron Devices Meeting (IEDM)* 1–4 (2021). doi:10.1109/IEDM19574.2021.9720508.
30. Mueller, S. *et al.* From MFM Capacitors Toward Ferroelectric Transistors: Endurance and Disturb Characteristics of HfO₂-Based FeFET Devices. *IEEE Trans. Electron Devices* **60**, 4199–4205 (2013).

31. Zhang, X. *et al.* Single-crystalline BaTiO₃-based ferroelectric capacitive memory via membrane transfer. *Sci. Adv.* **11**, eadz2553 (2025).
32. Toprasertpong, K., Takenaka, M. & Takagi, S. Memory Window in Ferroelectric Field-Effect Transistors: Analytical Approach. *IEEE Trans. Electron Devices* **69**, 7113–7119 (2022).
33. Pramanick, A., Prewitt, A. D., Forrester, J. S. & Jones, J. L. Domains, Domain Walls and Defects in Perovskite Ferroelectric Oxides: A Review of Present Understanding and Recent Contributions. *Crit. Rev. Solid State Mater. Sci.* **37**, 243–275 (2012).
34. Shin, Y.-H., Grinberg, I., Chen, I.-W. & Rappe, A. M. Nucleation and growth mechanism of ferroelectric domain-wall motion. *Nature* **449**, 881–884 (2007).
35. Liu, S., Grinberg, I. & Rappe, A. M. Intrinsic ferroelectric switching from first principles. *Nature* **534**, 360–363 (2016).
36. Yang, J. Theoretical Lower Limit of Coercive Field in Ferroelectric Hafnia. *Phys. Rev. X* **15**, (2025).
37. Lenox, M. K., Jaszewski, S. T., Fields, S. S., Shukla, N. & Ihlefeld, J. F. Impact of Electric Field Pulse Duration on Ferroelectric Hafnium Zirconium Oxide Thin Film Capacitor Endurance. *Phys. Status Solidi A* **221**, 2300566 (2024).

Acknowledgements

Y.L., T. C., and J. T. H. acknowledge partial support from the Intel FEINMAN 2.0 program. Y.L. and J. T. H. additionally acknowledge partial support from the ONR grant N000142612047. This work was performed in part at the University of Michigan Lurie Nanofabrication Facility. HZO films were prepared under support from the Laboratory Directed Research and Development Program at Sandia National Laboratories. Sandia is a multimission laboratory managed and operated by National Technology and Engineering Solutions of Sandia LLC, a wholly owned subsidiary of Honeywell International Inc. for the U.S. Department of Energy's National Nuclear Security Administration under Contract No. DE-NA0003525.

Author contributions

J. T. H. conceived the project and coordinated the studies. Y. L. and T. C. performed the device fabrication and electrical measurements. J. T. H. and Y. L. formulated the model, carried out the fitting, simulations and analysis. M. K. L. and J. F. I. synthesized the HZO sample. J. P. synthesized the BTO sample. W. S. provided scientific insights. Y. L. and J. T. H. wrote the manuscript. All authors proofread and commented on the manuscript.

Declaration of competing interests

The authors declare no competing interests.

Supplementary information for
Ferroelectric dynamic-field-driven nucleation and growth model for predictive materials-to-circuit co-design

Yi Liang,^{1,5,*} Tony Chiang,¹ Megan K. Lenox,² John J. Plombon,³ Jon F. Ihlefeld,^{2,4} Wenhao Sun,¹ and John T. Heron^{1,5,*}

¹Department of Materials Science and Engineering,

University of Michigan, Ann Arbor, MI 48109, USA

²Department of Materials Science and Engineering,

University of Virginia, Charlottesville, VA 22904, USA

³Technology Research, Intel Corporation, Hillsboro, OR 97124, USA

⁴Charles L. Brown Department of Electrical and Computer Engineering,

University of Virginia, Charlottesville, VA 22904, USA

⁵The Ferroelectronics Laboratory, Ann Arbor, MI 48109, USA

* Corresponding authors: liangyy@umich.edu, jtheron@umich.edu

1. Deficiency of KAI model in capturing switching behavior under time-dependent voltage

KAI model describes the transformed fraction f of polarization at time t by:

$$f(t) = 1 - \exp \left[- \left(\frac{t}{t_0} \right)^n \right] \quad (S1)$$

where t_0 is the characteristic time related to voltage-independent nucleation rates and domain wall velocities, and n is the Avrami exponent related to domain growth dimension. The conventional form of the KAI model only applies to the constant electric field case. To involve voltage dependence, Merz law can be introduced to t_0 , i.e. $t_0(t) = t_\infty \exp \left[\frac{V_a}{V(t)} \right]$, so that

$$f(t) = 1 - \exp \left[- \left(\frac{t}{t_\infty \exp \left[\frac{V_a}{V(t)} \right]} \right)^n \right] \quad (S2)$$

t_∞ is the characteristic time at infinite voltage, V_a is the activation voltage of domain wall depinning, and $V(t)$ is the instantaneous voltage across the ferroelectric capacitor. With the voltage-dependent KAI model, the polarization response under the ramp (Fig. 1b, green dashed line) coalesces with that under constant bias (Fig. 1b, green solid line) once the set point is reached. This behavior is unphysical, as the applied voltage during the ramp remains below the set point prior to 10 ns, and the polarization would therefore be expected to require a longer time to reach the same value. Therefore, a model that captures the voltage path dependence is needed to correctly reflect the polarization switching physics.

2. Detailed derivation of DFNG model with voltage-dependent homogeneous nucleation rate

The voltage-dependent homogeneous nucleation rate is derived from the Janovec-Kay-Dunn model, which gives the probability of nucleation per site governed by thermodynamic barrier by $\exp\left(-\frac{\Delta G^*}{k_B T}\right)$ and ΔG^* is the critical Gibbs free energy to create a nucleus. Assuming a cylindrical nucleus that extends across the thickness and ignoring the depolarization field, ΔG^* is given by $\frac{\pi t_{FE}^2 \sigma^2}{2P_S V(\tau)}$ ^{1,2}. t_{FE} is the thickness of the ferroelectric layer, σ is the domain wall energy, P_S is the spontaneous polarization, and $V(\tau)$ is the instantaneous voltage when nucleation happens at time τ . Then the homogeneous nucleation rate at time τ is the product of site density, nucleation probability and dipole flipping attempt frequency ω_0 ³,

$$J_{Homo}(\tau) = \rho \omega_0 \exp\left[-\left(\frac{\pi t_{FE}^2 \sigma^2}{2P_S V(\tau) k_B T} + \frac{V_a}{V(\tau)}\right)\right], \quad (S3)$$

where ρ is the homogeneous nucleation density. At constant temperature, the expression of $\langle N(t) \rangle$ becomes:

$$\langle N(t) \rangle = B^d \int_0^t \exp\left[-\frac{V_a + \sigma'^2}{V(\tau)}\right] \left[\int_{\tau}^t \exp\left[-\frac{V_a}{V(t')}\right] dt' \right]^d d\tau, \quad (S4)$$

where $B^d = \gamma \rho \omega_0 v_0^d$, $\sigma'^2 = \frac{\pi t_{FE}^2 \sigma^2}{2P_S k_B T}$.

In material systems where heterogeneous (instantaneous) and homogeneous nucleation coexist, $\langle N(t) \rangle$ is given by summing eqn. (3) and (4), and hence needs 5 fit parameters:

$$\langle N(t) \rangle = A^d \left[\int_0^t \exp\left[-\frac{V_a}{V(t')}\right] dt' \right]^d + B^d \int_0^t \exp\left[-\frac{V_a + \sigma'^2}{V(\tau)}\right] \left[\int_{\tau}^t \exp\left[-\frac{V_a}{V(t')}\right] dt' \right]^d d\tau. \quad (S5)$$

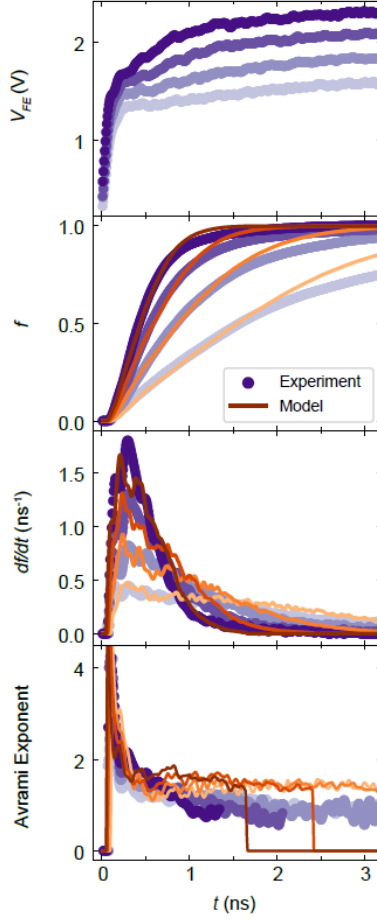


Figure S1: Fitting HZO transients with both heterogeneous and homogeneous nucleation. The experimental transients of a 3 μm diameter HZO capacitor is fit to the model using eqn. (S5) with 5 parameters, including heterogeneous and homogeneous nucleation terms. The model yields parameters $d = 0.808 \pm 0.004$, $V_a = 11.68 \pm 0.12 \text{ V}$, $\sigma'^2 = 42.87 \pm \infty \text{ V}$, $A = 1918 \pm 138 \text{ ns}^{-1}$, and $B = 1587 \pm \infty \text{ ns}^{-\frac{1}{d}-1}$. Despite that the modeled data (orange) matches relatively well to the experimental data (purple), the model cannot produce a converged solution to parameter σ'^2 and B . Moreover, the unreasonably high domain wall energy indicates that homogeneous nucleation is unlikely in the HZO system. Therefore, the polarization switching in HZO is solely dominant by heterogeneous nucleation.

3. The extraction of material parameters for BTO

Following the fit procedure in Methods, the experimentally measured switching transients of a 3 μm BTO capacitor is fit to the model, as shown in Fig. S2. The extracted parameters are $d = 1.144 \pm 0.004$, $V_a = 0.536 \pm 0.003 \text{ V}$, $\sigma'^2 = 1.47 \pm 0.04 \text{ V}$, $A = 6.13 \pm 0.07 \text{ ns}^{-1}$, and $B = 713 \pm 44 \text{ ns}^{-\frac{1}{d}-1}$. Specifically, the Avrami exponent of BTO shows a distinct behavior compared to HZO, which comes from the contribution of homogeneous nucleation. The universal applicability of the model under dynamic field is manifested by good fits to the switching transients of both polycrystalline materials and single crystalline materials under various distorted waveforms. The reduction of the growth dimension d from the physical device dimensions (2D) can be attributed to impediment of the domain wall motion in the system such as the finite size effects, grain boundaries and defects, which produces a truncated time cone⁴. The truncated time cone also accounts for the deviation between the model and the experimental data when approaching the end of the switching. Besides a higher growth dimension compared to HZO, BTO also exhibits a much lower Merz barrier (V_a) and heterogeneous nucleation density (A). The domain wall energy σ of BTO is derived to be $\sim 4.4 \text{ mJ/m}^2$, according to $\sigma'^2 = \frac{\pi t_{FE}^2 \sigma^2}{2P_S k_B T}$, and using $P_S = 20 \mu\text{C/cm}^2$, $t_{FE} = 20 \text{ nm}$, $T = 300 \text{ K}$. The domain wall energy derived by our model is comparable to *ab initio* calculated values⁵. Homogeneous nucleation density is estimated as $\sim 10^{-4} \text{ nm}^{-d}$ using a dipole attachment frequency ω_0 of 1 THz⁶, and v_0 of 5000 m/s⁷. It reveals that nucleation in BTO is sparse and that the domains are large (100s-1000s nm).

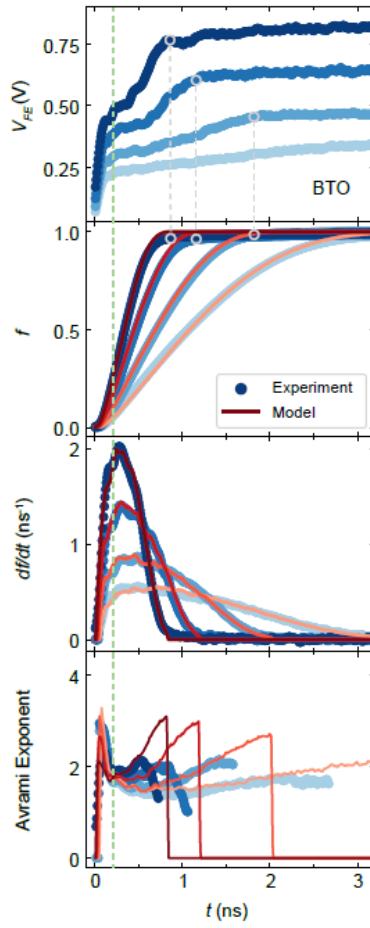


Figure S2: Model fit of a 3 μm BTO capacitor. Experimentally measured voltage (V_{FE}), transformed fraction (f), normalized ferroelectric switching current ($d\bar{f}/dt$) and Avrami exponent of a 3 μm diameter single crystalline BTO capacitor as a function of time (blue) along with the model fit from 5 free parameters (red). The green dashed vertical lines label the time when the fast voltage ramp from the supply finishes (~ 200 ps). The time between the green dashed vertical line and the grey dashed vertical lines encloses the distorted voltage waveform due to the circuit effect. The grey circles mark the corresponding transformed fraction at the time the voltage saturates to the setpoint.

4. Parameter space exploration and application metrics extraction

4.1 Simulation of hysteresis loops

Leakage, linear dielectric constant, and depolarization in the ferroelectric capacitor are ignored and a preset $-P_S$ state is assumed. The method to generate the polarization switching during a voltage ramp is shown in Fig. S3a and S3b, which is essentially half of a hysteresis loop. The voltage ramp is described by $V_{FE}(t) = V_0 \cdot \frac{1}{T/4} \cdot t$. T is the period of the hysteresis loop, and the frequency F of the loop is given by $1/T$. V_0 is the set voltage of the ramp. The frequency of the loops in Fig. 4a is 1 MHz, and the set voltage is 3 V. The full hysteresis loop is shown in Fig. S3c. The polarization only switches during 0-250 ns and 500-750 ns per the assumption, and the switching transients in these two periods are asymmetric. Interestingly, this method can be used to generate frequency dependent hysteresis loop. The frequency dependent coercive voltage (V_C) matches the empirical power law $V_C \propto F^\beta$ ⁸ (Fig. S4).

For parameter space exploration, we iterate every combination of parameters among $d = 0.6, 0.8, 1.0, 1.2, 1.4, 1.6, 1.8$; $V_a = 4, 8, 13, 18$ V; $A = 10, 10^2, 5 \times 10^2, 10^3, 5 \times 10^3, 10^4, 5 \times 10^4, 10^5$ ns⁻¹.

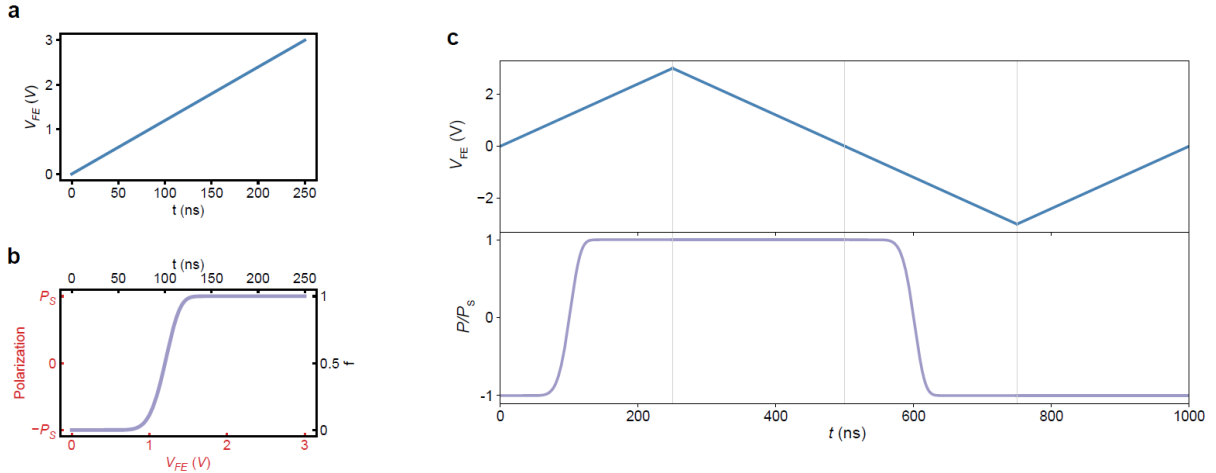


Figure S3: Hysteresis loop generation. **a**, The voltage ramp of a 1 MHz hysteresis loop. **b**, The transformed fraction f as a function of time can be mapped to the polarization as a function of voltage. The ferroelectric polarization is preset to $-P_S$, and switches to P_S during the voltage ramp, corresponding to a transformed fraction from 0 to 1. **c**, The full waveform of a hysteresis loop measurement and the corresponding polarization values.

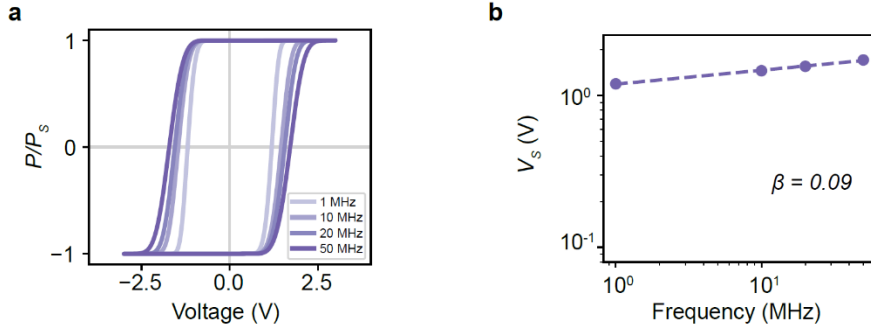


Figure S4: Frequency dependent hysteresis loops. **a**, Simulated hysteresis loops under 1, 10, 20, 50 MHz triangular waveform. **b**, Frequency dependent coercive voltage. Using the parameter sets of the 3 μm HZO capacitor, the model captures the empirical power law $V_C \propto F^\beta$. The dots are simulated coercive voltages, and the dashed line is a linear fit. The linear fit gives a β value of 0.09.

4.2 Extraction of application metrics and grading of the loops

Instead of triangular waves and linear ramp of voltages, pulse waveforms are more commonly used in circuits operations for higher latency. All simulated pulse waveforms used in this work are defined as $V_{FE}(t) = \frac{2}{\pi} V_0 \arctan 50t$. V_0 is the pulse amplitude. This equation gives a rise time of ~ 80 ps to reach $\sim 0.85 V_0$. A simulation example is shown in Fig. S5.

To grade the loops according to the procedure mentioned in the main text, we first simulate the switching transient under a pulse operation of 1.5 V for every parameter set involved. Then we select the parameter sets that allow more than 99% switching fraction at 10 ns. The voltage when $f=0.99$ is minimum pulse amplitude required (V_{min}). We run the simulation again under a pulse with an amplitude of V_{min} to extract the delay, which is the time needed to complete 99% switching transformation, as well as under a pulse with an amplitude of $V_{min}/2$ and a width of the delay to extract Δf (normalized disturbed polarization in $V_{DD}/2$ write scheme).

For FeCap and FeFET devices, the key metrics are memory windows, namely the capacitance (C_{norm}) and coercive voltage (V_C), respectively. These two quantities are highly susceptible to the frequency of the electrical waveform, or equivalently the ramp rate of the voltage under a variety of application contexts. As a proof-of-concept, we extract these two values using a fast voltage ramp of 0.1 V/ns, which is approximate to a 320 MHz, 0.05 V AC small signal oscillation.

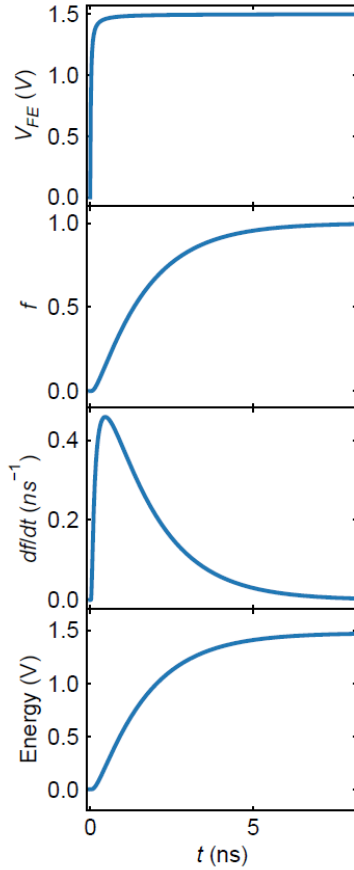


Figure S5: Simulated switching transient under pulse waveform. In this simulation, V_0 is set to be 1.5 V. After calculating the transformed fraction f and then the normalized ferroelectric current df/dt , energy is given by integrating the product of df/dt and V_{FE} over time.

5. Parameter sets filtering for FeFETs and FeCaps

We use a nominal criterion of $V_C \geq 1.4$ V to select favorable FeFETs gate materials. It is inferred from Fig. 4b that only the delay has a broad distribution and needs consideration under this selection. Table S1 is a table of the satisfying parameter sets, in the order of increasing delay. The parameter set that gives the minimum delay is highlighted in orange. The one that is closest to our measured HZO sample is highlighted in blue. It indicates a possible solution that if the depinning field is relatively unchanged, by slightly increasing the growth dimension (for example through geometric design or removing grain boundaries) and nucleation density (for example by introducing point defects), the HZO can be more suitable for FeFETs. Moreover, the parameter set highlighted in green also provides a potentially viable solution that by diminishing the pinning defects (and therefore increasing d , and reducing V_a and A), HZO can be adapted to fit the device need.

$C_{norm} \geq 12 \text{ V}^{-1}$ is selected for FeCap devices. From Fig. 4b, this criterion gives small delay but a wide distribution in other metrics. If Δf is required to be less than 1%, only three sets of parameters satisfy the standard (Table S2). These parameter sets have high growth dimension approaching the physical dimension (2D) and small depinning field, which is more aligned with single crystalline materials. However, the nucleation density needs to maintain high. The demanding values and the rarity of suitable parameters indicate polycrystalline materials are probably not ideal for FeCaps.

d	V_a (V)	A (ns $^{-1}$)	Delay (ns)	V_c (V)
1.8	13	5000	3.25	1.44
1.6	13	5000	3.56	1.44
1.4	13	5000	4.01	1.44
1.8	18	100000	4.54	1.52
1.2	13	5000	4.73	1.43
1.6	18	100000	4.98	1.52
1.8	8	100	5.24	1.45
1.4	18	100000	5.62	1.52
1.6	8	100	5.79	1.45
1.0	13	5000	5.95	1.42
1.4	8	100	6.58	1.44
1.2	18	100000	6.61	1.51
1.2	8	100	7.83	1.43
1.0	18	100000	8.33	1.51
1.8	18	50000	8.44	1.60
0.8	13	5000	8.48	1.41
1.6	18	50000	9.30	1.60
1.0	8	100	9.98	1.42

Table S1: Favorable parameters for FeFETs.

d	V_a (V)	A (ns $^{-1}$)	C_{norm} (V $^{-1}$)
1.6	4	10000	12.51
1.8	4	5000	12.37
1.8	4	10000	14.06

Table S2: Favorable parameters for FeCaps.

1. Janovec, V. On the theory of the coercive field of single-domain crystals of BaTiO₃. *Czech J Phys* **8**, 3–15 (1958).
2. Kay, H. F. & Dunn, J. W. Thickness dependence of the nucleation field of triglycine sulphate. *The Philosophical Magazine: A Journal of Theoretical Experimental and Applied Physics* **7**, 2027–2034 (1962).
3. Deck, L.-T. & Mazzotti, M. Conceptual Validation of Stochastic and Deterministic Methods To Estimate Crystal Nucleation Rates. *Crystal Growth & Design* **23**, 899–914 (2023).
4. Concurrent Nucleation and Growth. in *Kinetics of Materials* 533–542 (John Wiley & Sons, Ltd, 2005). doi:10.1002/0471749311.ch21.
5. Meyer, B. *Ab initio* study of ferroelectric domain walls in PbTiO₃. *Phys. Rev. B* **65**, (2002).
6. Hlinka, J. *et al.* Soft-mode spectroscopy of epitaxial BaTiO₃/SrTiO₃ superlattices. *Phys. Rev. B* **82**, 224102 (2010).
7. Kashida, S., Hatta, I., Ikushima, A. & Yamada, Y. Ultrasonic Velocities in BaTiO₃. *J. Phys. Soc. Jpn.* **34**, 997–1001 (1973).
8. Chen, Z., Zhang, Y., Li, S., Lu, X.-M. & Cao, W. Frequency Dependence of the Coercive Field of 0.71Pb(Mg_{1/3}Nb_{2/3})O₃-0.29PbTiO₃ Single Crystal from 0.01 Hz to 5 MHz. *Appl. Phys. Lett.* **110**, 202904 (2017).

